Preprints.org

Article

Evaluation of a High Resolution WRF Model for Southeast Brazilian Coast: The Importance of Physical Parameterization to Wind Representation

Layrson Gonçalves [*] , Júlia Kaiser , Ronaldo Palmeira , Marcos Gallo , Carlos Eduardo Parente

Article

Evaluation of a High Resolution WRF Model for Southeast Brazilian Coast: The Importance of Physical Parameterization to Wind Representation

Layrson Gonçalves [1],*,‡ (ID)**, Júlia Kaiser** [1],‡ (ID)**, Ronaldo Palmeira** [2],‡ (ID)**, Marcos Gallo** [3],‡ (ID) **and Carlos Eduardo Parente** [3],‡ (ID)

[1]   Ocean Engineering Program, Federal University of Rio de Janeiro, Rio de Janeiro, Brazil; layrsongoncalves@gmail.com; js.kaiser@oceanica.ufrj.br

[2]   AtmosMarine Consultoria e Tecnologia; Rio de Janeiro, Brazil; ronaldo@atmosmarine.com

[3]   Ocean Engineering Program, Federal University of Rio de Janeiro, Rio de Janeiro, Brazil; marcosgallo@oceanica.ufrj.br; parente@oceanica.ufrj.br

*   Correspondence:layrsongoncalves@gmail.com

‡   These authors contributed equally to this work.

Abstract: This study assesses the performance of the Weather Research and Forecasting (WRF) model using a high-resolution spatial grid (1 km) with various combinations of physical parameterization packages to simulate a severe event in August 2021 in the southeastern Brazilian coast. After determining the optimal set of physical parameterizations for representing wind patterns during this event, a year-long evaluation was conducted, covering forecast horizons of 24, 48, and 72 hours. The simulation results were compared with observational wind data from four weather stations. The findings highlight variations in the efficacy of different physical parameterization sets, with certain sets encountering challenges in accurately depicting the peak of the severe event. The most favorable results were achieved using a combination of Tiedtke (cumulus), Thompson (microphysics), TKE (boundary layer), Monin-Obukhov (surface layer), Unified-NOAH (land surface), and RRTMG (shortwave and longwave radiation). Over the one-year forecasting period, the WRF model effectively represented the overall wind pattern, including forecasts up to three days in advance (72-hour forecast horizon). Generally, the statistical metrics indicate robust model performance, even for the 72-hour forecast horizon, with correlation coefficients consistently exceeding 0.60 at all analyzed points. While the model proficiently captured wind distribution, it tended to overestimate northeast wind speed and gust intensities. Notably, forecast accuracy decreased as stations approached the ocean, exemplified by the ATPM station.

Keywords: WRF model; Wind simulation; Parameterizations

---

1. Introduction

The knowledge of meteorological conditions plays a role in various aspects of our lives. This comprehension contributes to everything from planning our daily activities to the consistent functioning of industries like agriculture, transportation, and the energy sector. There is an exponentially increasing demand for understanding wind patterns at various locations due to the growing utilization of wind energy for power production. However, it is essential to understand that this knowledge is also of fundamental importance for security reasons. The increase in intensity and frequency of extreme events is a reality that has been observed in various parts of the world [1], and we must be prepared to face it.

According to [1], there is an alteration in the pattern of extreme winds driven by changes in the geographic distribution, frequency, and intensity of extreme weather events, which includes tropical cyclones, extra-tropical cyclones, and convective storms. These changes have the potential to result in more frequent and severe storms in certain regions across the world. In that sense, some studies such as [2–5], and [6] indicated that global mean and extreme wind conditions may have experienced an increase. For example, [5] investigated the climatology and trends winds and waves in the Arctic Ocean and showed a clear positive trend in surface wind speed over 20 years of altimeter observations

in some areas. More than that, the authors pointed out that extreme wind events are increasing and the wind fetch is becoming larger because of the ice retreat at Arctic Ocean. In the same perspective, [6] analyzed 33 years of satellite data and found positive trends in mean wind speed and even larger positive trends in the 90th percentile values over global oceans.

Coastal regions are among the most susceptible areas to bear the impacts of the frequent storms. [7] conducted an analysis of a significant rainfall event that occurred on March 17th-18th, 2013, impacting the coastal regions of São Paulo and Rio de Janeiro, as well as the mountainous region of Rio de Janeiro, Brazil. This extreme event was caused by the passage of a cold front accompanied by strong winds at lower altitudes. In Petrópolis (RJ), the accumulated precipitation over 24 hours was higher than 400 mm, while the coastal areas of Rio de Janeiro also recorded over 100 mm of accumulated precipitation. The study concluded [7] that accurately predicting the storm's intensity and precise location remains a challenge for numerical models.

[8]'s work shows that heavy rainfall combined with the geological attributes of the Baixada Santista Metropolitan Region in Brazil played a significant role in triggering the landslides, which caused displacement of residents, damage to local infrastructure and loss of lives. The authors focused the study in one of the most intense meteorological events of the recent years in the region and utilized meteorological satellite, radar data, and output from ERA5 reanalysis to analyze the atmospheric characteristics. The paper emphasizes the urgency of improving early warning systems to mitigate the impacts of future driven by foreseeable meteorological conditions.

Another noteworthy example of extreme weather event occurred in the state of Espírito Santo (ES), Brazil on November 2010. This event was a severe thunderstorm that generated wind gusts exceeding 100 km/h, leading to significant economic losses. Further details about this event can be found in the study by [9]. In their study, the authors described an operational hydrometeorological forecast system designed for ES, developed in response to the aforementioned extreme event, with the aim of improving its nowcasting capabilities. [9] draw attention to, among other things, the need for ultra high resolution numerical weather prediction systems, higher spatial and temporal resolution monitoring systems, integrated environmental information systems, and advanced science and technology in order to develop better diagnostic and prognostic weather products.

In that sense, [10] assessed the performance of the WRF model in a brazilian tropical region, with a specific emphasis on wind representation. The authors emphasized the significance of such investigations to adequately support the expanding utilization of wind energy as an important source for the energy matrix of many countries. The results highlighted the WRF model's ability to depict the overall wind speed patterns, albeit with a tendency to overestimate the observed data. A noteworthy conclusion of this study is that proximity to the ocean degraded the accuracy of the model simulations, highlighting the complex characteristics of the coastal regions to atmospheric model simulations.

Considering that the lack of observational data remains a concern, particularly in developing countries, work with well calibrated atmospheric models is fundamental. In this context, the main objective of this study is to identify the optimal parameterization scheme for a high-resolution regional model, improving its capacity to accurately represent the wind patterns in a region along the southeastern Brazilian coast. Based on this, a one-year simulation is carried out to assess the modeling accuracy for the area of interest across various forecast horizons. The remaining content is structured in the following manner: Section 2 introduces the study area, outlines the model configuration, and presents the statistical metrics to be used to evaluate the model performance. Furthermore, it provides a comprehensive event description along with specific information about model configurations for each simulation. The results are exhibited in Section 3. In this section, the reader can access the results of the parameterization tests, as well as those from the extended simulation. The discussion and conclusions follow in Section 4.

2. Materials and Methods

2.1. Study Area

Espírito Santo, located in southeastern Brazil as exhibited in Figure 1, showcases varied geography with coastal plains, mountain ranges, and plateaus. Its tropical monsoon climate exhibits distinct wet (October to March) and dry (April to September) seasons, influencing precipitation patterns and temperature fluctuations. The region is susceptible to occasional extreme weather events, necessitating proactive measures and preparedness to mitigate potential impacts on its ecosystems and socio-economic activities [11].

In this region, wind directions and speeds at the synoptic scale are under the influence of the South Atlantic Subtropical Anticyclone (ASAS), Transient Systems (ST), and the South Atlantic Convergence Zone (ZCAS). [12] showed that during ASAS influence, winds from the north and northeast are frequent in the offshore region, while southern regions experience winds from the east. Under ST influence, the central sector experience frequent south winds, the northern sector has southeast winds, and the southern sector experience southwest winds. During ZCAS events, winds from the south, southeast, and southwest are significant, whereas pre-ZCAS and post-ZCAS periods have dominant winds from the north, northeast, and east.

On November 18, 2010, Tubarão Harbor located at ES experienced a severe thunderstorm event (the same mentioned in Section 1) that resulted in the destruction of two loading structures operated by VALE, a prominent Mining Company in South America. The incident was triggered by a rapidly moving cold front, generating super cells and wind gusts exceeding 100 km/h at approximately 11:00 p.m. UTC [9]. The disruptive weather event led to interruptions in shipping loading operations, causing considerable economic losses, with the potential for greater impact. In response, VALE has taken proactive steps to invest in weather forecasting, focusing on developing nowcasting capabilities to enhance preparedness for future weather events.

For the model performance evaluation, the wind measurements used were from 3 weather stations (ATPM, INVT and INVV) and one METAR system (MEVT). The stations named INVT and INVV are automatic weather stations (AWS) maintained by the brazilian National Institute of Meteorology (INMET). The locations of all the 4 stations are presented at Figure 1. Here, the wind data were taken at a height of 10 meters above the ground, and they were resampled at 1 hour intervals.
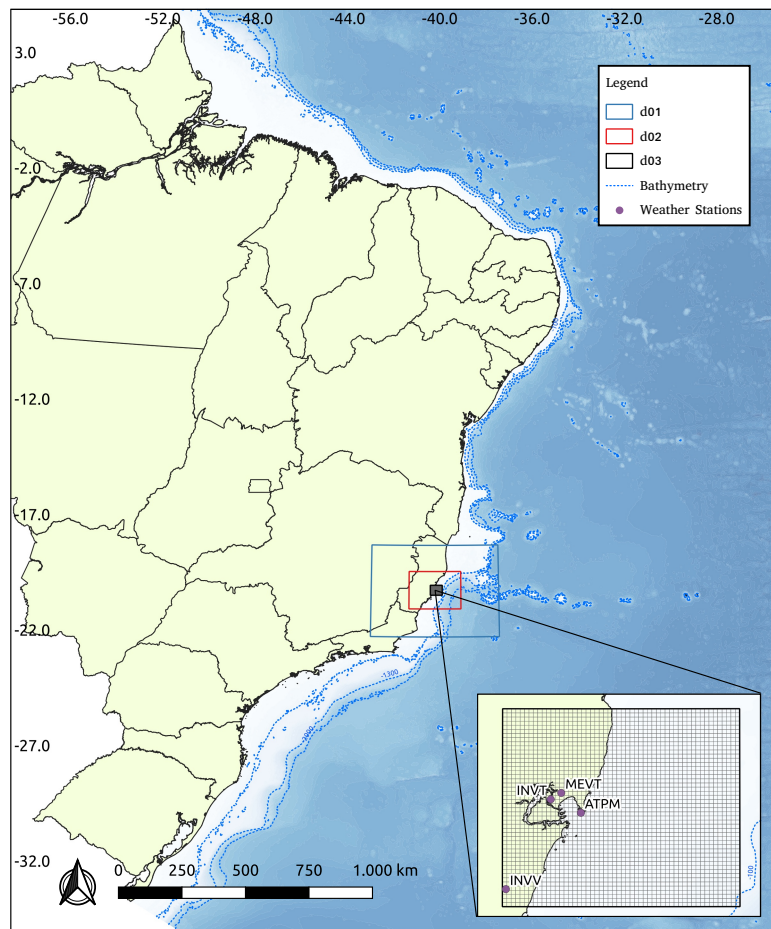
Figure 1. The 3 telescopic nested grids with resolutions 9km (d01), 3km (d02) and 1km (d03). The innermost domain (3th) has 55x161 grid points and 1km resolution centered at Tubarão Port Complex, Brazil. INVT, INVV, ATPM, and MEVT are the points of interest.

2.2. Model Configuration and Numerical Simulations

The weather forecast atmospheric model used in this work is the Weather Research and Forecasting (WRF). The WRF [13,14] was developed by the National Center for Atmospheric Research (NCAR) for research purposes and numerical weather forecasting. Currently, this model is widely used and improved by the scientific community and in operational meteorological centers of international importance, such as the National Center for Environmental Prediction (NCEP) located in the United States. In addition, in Brazil, WRF is also used in forecasts made by the National Institute for Space Research (INPE) and by the city of Rio de Janeiro (AlertaRio) in their regional simulations. The WRF is a mesoscale model with a non-hydrostatic dynamic core and numerous physical parameterization options available, from simpler parameterizations to more sophisticated ones [15]. Simulations can be performed with nested grids and initial and boundary conditions are usually obtained from global models such as the Global Forecast System (GFS).

For the purpose of the present study, the 4.2.2 version of WRF is used and the horizontal domain is configured with 3 two-way nested grids (Figure 1) with resolutions of 9, 3, and 1 km respectively and with 64 eta vertical levels. Table 1 shows the spatial coverage details of each nested grid. The initial and boundary conditions are derived from GFS, the global product from NCEP, at $0.25° \times 0.25°$ spatial resolution and 3 hours of temporal resolution. The model is initialized at 1200 UTC, and the first 12 h of simulation is considered the model spin-up period, and then it was discarded from the analysis presented here.

Table 1. Main characteristics of the grids used to atmopheric forecasts. $\Delta_{x,y}$ is the spatial resolution of the grids in degrees; N_x and N_y are the numbers of points in x and y axis, respectively; Lat_i is the initial latitude, Lon_i is the initial longitude, Lat_f is the final latitude, and Lon_f is the final longitude of the grids.

	Grid 1	Grid 2	Grid 3
$\Delta_{x,y}$	9 km	3 km	1 km
N_x	65	79	55
N_y	141	161	161
Lat_i	-22.68°	-21.22°	-20.50°
Lon_i	-43.37°	-41.46°	-39.90°
Lat_f	-18.02°	-19.37°	-20.08°
Lon_f	-37.13°	-38.99°	-40.11°

The simulation scheme is divided into two phases. The first phase focuses on evaluating the model's performance using various parameterization approaches for a 24-hour forecast depicting a specific severe event, whose characteristics are detailed in Subsection 2.3. Based on the parameterization that performs the best in phase 1, the second stage concentrates on assessing the model's performance across forecast horizons, ranging from 24 to 72 hours. So, on the first step, a set of 9 experiments were carried out for the period of August 28 up to September 2, 2021, when wind gusts recorded by an anemometer at Tubarão Harbor exceeded 70 km/h. The simulations were carried out for 36 h each day, and the first 12 hours of spin-up were discarded – only the subsequent 24 hours were analyzed on the scope of this study. The dynamics and physics schemes used in this investigation are given in Table 2. During phase 2, a year-long simulation was conducted considering a 84 hours run for each day. This approach ensures reliable outputs for the subsequent 72 hours after excluding the initial 12-hour spin-up period. The simulations of both stages were made using GFS as initial and boundary conditions.

Table 2. Physical parameterization schemes of the WRF model used to evaluate the forecast performance on the August 2021 event.

	Cumulus	MP	BL	SL	LS	LWR	SWR
T1	Tiedtke [16]	Thompson [17]	MYJ [18]	ETA [18]	Unified NOAH [19]	RRTMG [20]	RRTMG [20]
T2	Kain-Fritsch [21]	WSM 3-class [22]	YSU [23]	MM5-REV [24]	NOAH-MP [25]	RRTMG [20]	RRTMG [20]
T3	Kain-Fritsch [21]	Ferrier [26]	YSU [23]	MM5-REV [24]	NOAH-MP [25]	RRTMG [20]	RRTMG [20]
T4	Grell-Devenyi [27]	Ferrier [26]	YSU [23]	MM5-REV [24]	NOAH-MP [25]	RRTMG [20]	RRTMG [20]
T5	Kain-Fritsch [21]	Purdue Lin [28]	YSU [23]	MM5-REV [24]	NOAH-MP [25]	RRTMG [20]	RRTMG [20]
T6	Tiedtke [16]	WSM 6-class [29]	YSU [23]	MM5-REV [24]	NOAH-MP [25]	RRTMG [20]	RRTMG [20]
T7	Grell 3D [30]	WSM 3-class [22]	YSU [23]	MM5-REV [24]	NOAH-MP [25]	RRTM [31]	Dudhia [32]
T8	Kain-Fritsch [21]	Purdue Lin [28]	MY-NN3 [33]	MM5-REV [24]	NOAH-MP [25]	RRTMG [20]	RRTMG [20]
T9	Kain-Fritsch [21]	Ferrier [26]	MY-NN3 [33]	MM5-REV [24]	NOAH-MP [25]	RRTMG [20]	RRTMG [20]

MP = Microphysics; BL = Boundary layer; SL = Surface layer; LS = Land surface; LWR = Longwave radiation; SWR = Shortwave radiation.

2.3. Event Description

On August 30, 2021, a cold front rapidly displaced over the state of Espírito Santo (weather station data located at ATPM point in Figure 1). This advancement caused a drop in atmospheric pressure from 1023 hPa on August 28th to 1017 hPa on August 30th. A slight decrease in temperature was observed, and precipitation occurred with more than 50 mm in 24 hours, with a rate exceeding 20 mm per hour. The wind during the passage of the frontal system was from the west-southwest, later shifting to the south direction, when the most intense winds occurred, with gusts exceeding 70 km/h, as observed in the meteogram in Figure 2.
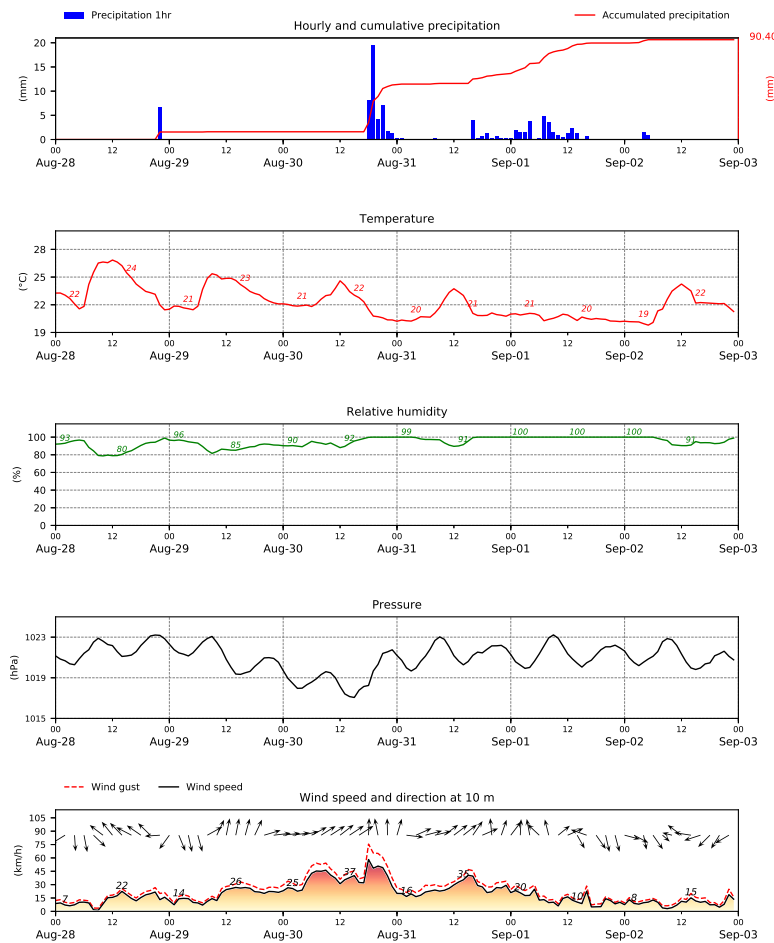
Figure 2. Meteogram illustrating the meteorological conditions for the case study period (from August 28 to September 2, 2021), located at ATPM point in Figure 1 . The top panel (**a**) shows hourly precipitation data and the accumulated precipitation for the period of interest. The second (**b**), third (**c**) and fourth (**d**) panels presents temperature, relative humidity and pressure information, respectively. The bottom panel (**e**) displays wind speed, wind direction (black arrows) and wind gust (red dotted line) data.

2.4. Statistical Analysis

The performance of the model was evaluated using the statistical metrics Pearson's correlation coefficient (CORR), bias (BIAS), normalized bias (NBIAS), root mean square error (RMSE), normalized root mean square error (NRMSE), and scatter index (SI) - equations 1, 2, 3, 4, 5, and 6, respectively. In this context, CORR serves as an indicator of the model's capacity to track the observational trends - ideally, this value should be 1. Positive BIAS values indicate an overestimation of the simulated data, whereas negative values indicate underestimation. The RMSE parameter quantifies the overall error of the model, with lower values signifying higher model accuracy. The scatter index points the percentage error relative to average values and it is calculated to check the level of confidence in the model's results. We will employ these statistical metrics to assess the model's capability in representing the wind speed and gust patterns at the interested sites. Additionally, wind roses will be utilized to check the model's directional performance.

$$CORR = \frac{\sum_{i=1}^{n}(x_i - \bar{x})(y_i - \bar{y})}{\sqrt{\sum_{i=1}^{n}(x_i - \bar{x})^2 \sum_{i=1}^{n}(y_i - \bar{y})^2}}$$

(1)

$$BIAS = \frac{\sum_{i=1}^{n}(y_i - x_i)}{n} \tag{2}$$

$$NBIAS = \frac{\frac{\sum_{i=1}^{n}(y_i - x_i)}{n}}{\sqrt{\frac{\sum_{i=1}^{n} x_i^2}{n}}} \tag{3}$$

$$RMSE = \sqrt{\frac{\sum_{i=1}^{n}(y_i - x_i)^2}{n}} \tag{4}$$

$$NRMSE = \sqrt{\frac{\sum_{i=1}^{n}(y_i - x_i)^2}{\sum_{i=1}^{n}(x_i)^2}} \tag{5}$$

$$SI = \frac{\sqrt{\frac{1}{n}\sum_{i=1}^{n}[(y_i - \bar{y}) - (x_i - \bar{x})]^2}}{\bar{x}} \tag{6}$$

Where, N represents the number of sample data, y_i represents the i-th predicted value, x_i represents the i-th reference value (observed data), and $\bar{y}$ and $\bar{x}$ represent the mean values of the predicted and observed data, respectively.

3. Results

The results have been analyzed in accordance with the simulation scheme structure. In the initial section, we assess the performance of WRF model over a 24-hour forecast horizon during a 6-day period using 9 distinct sets of physical parameterizations. After that, in the second phase, we present the results derived from one-year model simulation, considering forecast horizons of 24, 48, and 72 hours, using the parameterization set that exhibited the most favorable results during the initial phase.

3.1. Assessing Model's Performance during August 2021's Event

From the analysis of temporal evolution of wind speed and gust during the August 2021's event (Figure 3), it is clear that all simulations align with the observed data trends. Specifically, there is a notable increase in wind intensities starting on August 30, culminating in peak values on August 31, followed by a subsequent decrease in wind speeds on September 1st. Nevertheless, it is worth noting that certain WRF's simulations face difficulties in accurately representing the peak of the event, resulting in an underestimation of observed wind speeds and gusts. To discern the simulation with the optimal performance among the nine tested configurations, we present a Taylor Diagram in Figure 4. In this context, simulation T1, which incorporates the Tiedtke scheme for cumulus parameterization, Thompson for microphysics, and RRTM parameterization for longwave and shortwave radiation fluxes, presents the better overall performance. This conclusion is based on the achievement of the highest correlation coefficients for both wind speed (0.84) and gusts (0.82), along with minimized errors as can be seen in Figure 4.
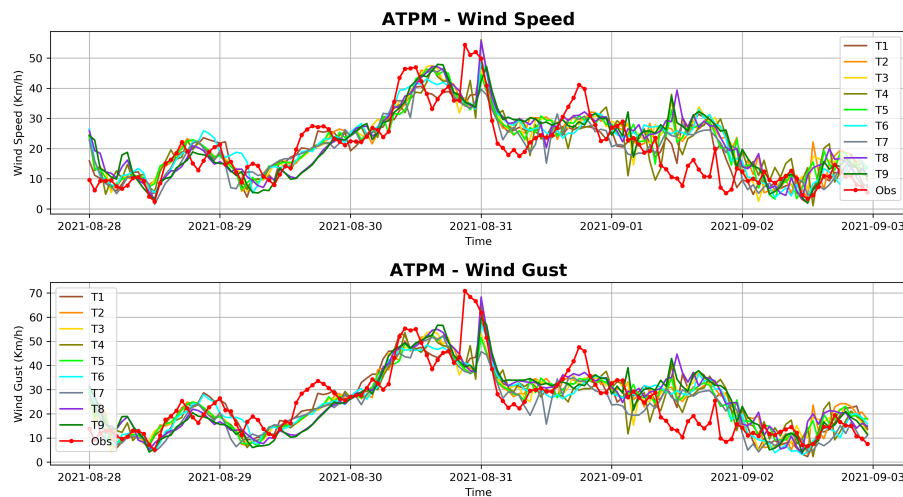
Figure 3. Time series (from August 28, 2021, to September 3, 2021) of wind speed (upper panel) and gusts (lower panel) obtained with the WRF model using 9 different sets of physical parameterizations for the point designated as ATPM. This time series was constructed using a 24-hour forecast horizon.
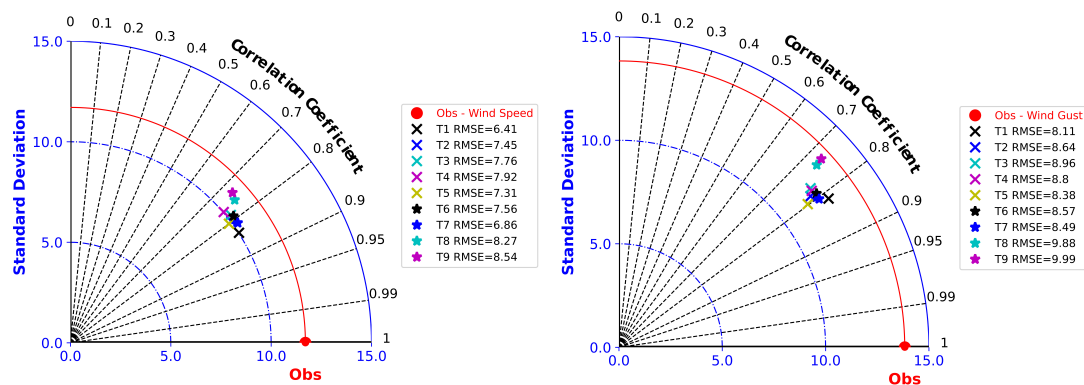

Figure 4. Statistical summary based on the Taylor Diagram for wind speed (left panel) and wind gusts (right panel) obtained from simulations with the WRF model using 9 different sets of physical parameterizations. The period considered is from August 28, 2021, to September 3, 2021, and the time series was constructed considering a 24-hour forecast horizon.

The superior performance of the T1 parameterization set must be related to the characteristics of each chosen parameterization. For instance, the Tiedtke scheme [16], based on mass flux, used to represent processes related to the generation, evolution, and dissipation of cumulus-type clouds, is more suitable for areas in tropical and subtropical regions where deep convection is a significant component of active atmospheric systems.

As for the chosen microphysics scheme, Thompson was selected. This scheme is responsible for modeling processes related to cloud particles, such as the formation of water droplets, growth of ice crystals, and other microphysical processes. The Thompson microphysics scheme [17] is indicated for regions with the presence of deep convective clouds, with high vertical development and cold tops. This corroborates with the findings by [34], which showed that, in the evaluation of 9 types of

microphysics schemes using the WRF model for the Southern region of Brazil, the Thompson scheme exhibited the best performance in locating convective cores for the region.

The RRTM radiation scheme [35] is responsible for rapidly calculating radiative transfer in the atmosphere, including the absorption and emission of radiation by atmospheric gases using the correlated-k distribution method. This method resolves spectral integration in each band with complex absorption lines through a simple formulation using a smooth function. This function follows the cumulative distribution formulation built from a set of absorption coefficients from a line-by-line model. The main advantage of using this scheme is that solving the Radiative Transfer Equation (RTE) becomes computationally more efficient compared to other methods because absorption coefficients are pre-calculated, reducing computational cost.

3.2. Assessing Model's Performance over a Year Long Simulation Period

After pointing out the optimal WRF configuration for the event, we conducted a year-long simulation spanning from October 2020 to September 2021. This simulation allowed us to evaluate the model's performance across 24-hour, 48-hour, and 72-hour forecast horizons. In this context, Figure 5 illustrates the scatter plots generated for the 24-hour wind speed forecast horizon, while Figure 6 exhibits the scatter plots obtained for wind gusts results. In all diagrams, the model output is presented on y-axis and the observations are presented on x-axis. As can be seen, for 24 hours forecast, the model tends to slightly overestimate low wind speeds at all points and underestimate the high wind speeds. Despite that, the average BIAS is always lower than 5 km/h - actually, for three of the four points it is lower than 3 km/h. On the performance of the model to represent the wind gusts, the model pattern is the same. Here, RMSE values are between 8 km/h and 10 km/h for all sites. It is important to note that there are no results for wind gusts at MEVT point due to the lack of observational data throught METAR system.
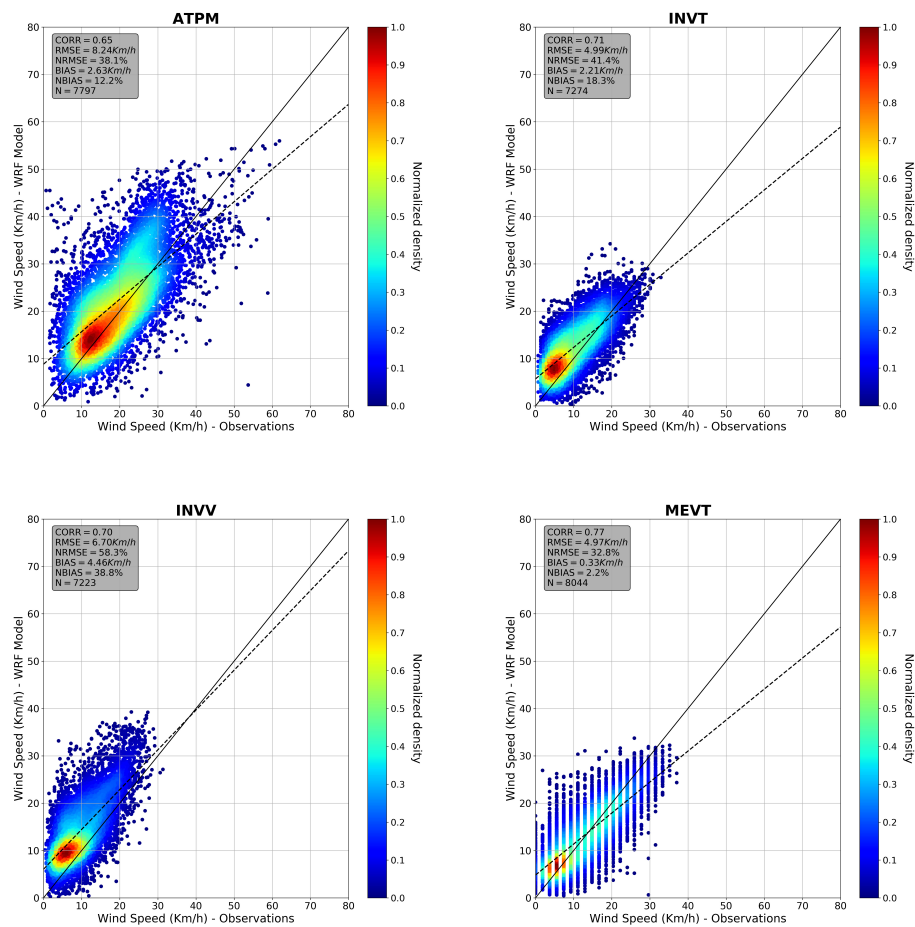
Figure 5. Scatter plots depicting the relationship between model output (24-hour forecast) for wind speed and the observations. The upper left panel displays the results for point ATPM while the upper right displays the results for point INVT; The bottom left panel displays the results for point INVV, and the bottom right panel displays the results for point MEVT.
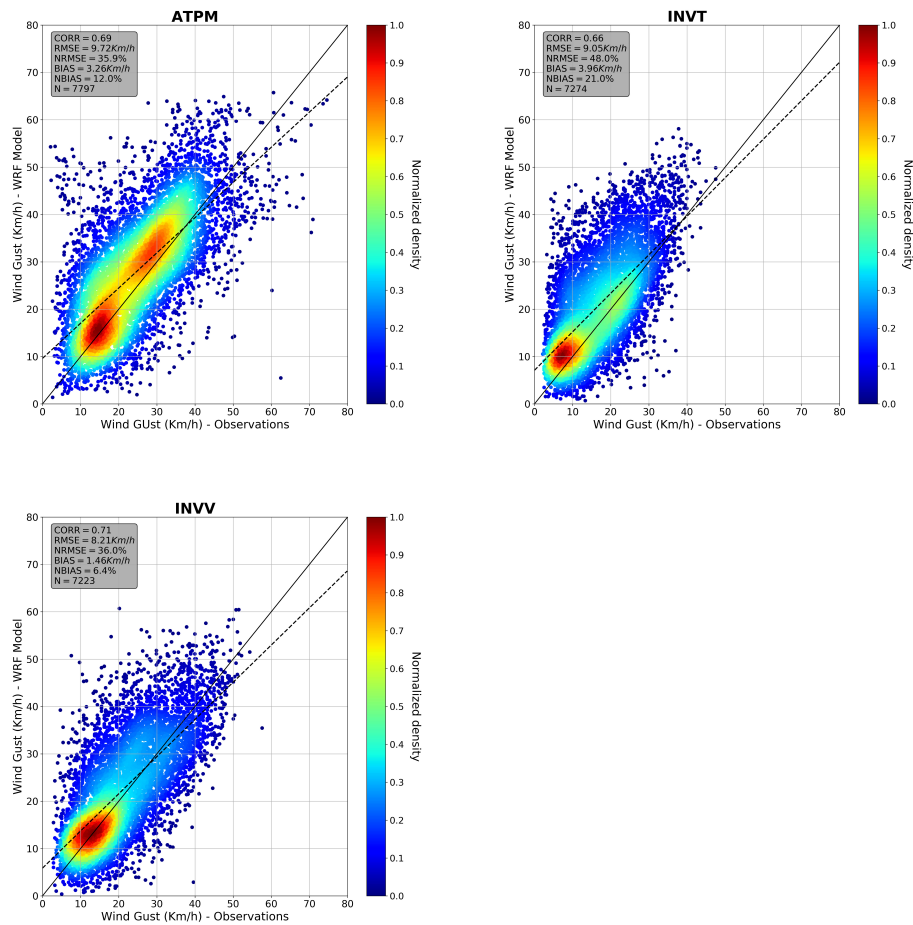
Figure 6. Scatter plots depicting the relationship between model output (24-hour forecast) for wind gust and the observations. The upper left panel displays the results for point ATPM while the upper right displays the results for point INVT; The bottom left panel displays the results for point INVV.

The overall statistics for all interested points considering the three forecast horizons (24-hour, 48-hour, and 72-hour) are detailed in Table 3. As expected, forecast errors increase as the forecast horizon extends. The largest model errors were observed at ATPM station, where the RMSE values ranged from 8.24 km/h (9.72 km/h) to 8.71 km/h (10.78 km/h) for wind speed (wind gust) parameter over the 24-hour to 72-hour forecast horizon. Conversely, the lowest model errors occurs for INVT station, where RMSE errors reached only 5.18 km/h for wind speed and 9.46 km/h for the 72-hour forecast horizon. Additionally, for the 24-hour forecast horizon, the lowest correlation coefficients were recorded at 0.65 for wind speed and 0.66 for wind gust. Notably, the simulation demonstrated the ability to achieve a wind speed correlation coefficient as high as 0.77 at the MEVT station.

Table 3. Summaries of the statistics obtained between the WRF model results and observed data for the 4 points of interest, considering forecast horizons of 24, 48, and 72 hours.

		CORR	BIAS (km/h)	NBIAS (%)	RMSE (km/h)	NRMSE (%)	SI (%)
ATPM	Wspd - 24h	0.65	2.63	12.20	8.24	38.1	40.67
	Gust - 24h	0.69	3.26	12.00	9.72	35.90	37.94
	Wspd - 48h	0.62	2.71	12.40	8.61	39.6	43.26
	Gust - 48h	0.64	3.63	13.30	10.56	38.80	41.85
	Wspd - 72h	0.60	2.47	11.30	8.71	40,0	43.88
	Gust - 72h	0.62	3.40	15.50	10.78	39.50	42.85
INVT	Wspd - 24h	0.71	2.21	18.30	4.99	41.4	42.9
	Gust - 24h	0.66	3.96	21.00	9.05	48.00	38.5
	Wspd - 48h	0.69	2.41	20.00	5.20	43.10	46.00
	Gust - 48h	0.64	4.30	22.80	9.41	49.90	39.90
	Wspd - 72h	0.69	2.31	19.20	5.18	43.00	46.20
	Gust - 72h	0.63	4.10	21.70	9.46	50.1	40.20
INVV	Wspd - 24h	0.70	4.46	38.80	6.70	58.30	49.90
	Gust - 24h	0.71	1.46	6.40	8.21	36.00	39.40
	Wspd - 48h	0.67	4.66	40.60	7.03	61.2	54.10
	Gust - 48h	0.68	1.78	7.80	8.85	38.80	39.50
	Wspd - 72h	0.66	4.66	40.70	7.07	61.70	54.80
	Gust - 72h	0.66	1.76	7.70	9.12	40.10	44.80
MEVT	Wspd - 24h	0.77	0.33	2.20	4.97	32.80	38.10
	Wspd - 48h	0.74	0.57	3.80	5.32	35.10	42.00
	Wspd - 72h	0.74	0.57	2.70	5.35	35.30	42.30

Figure 7, Figure 8, Figure 9, and Figure 10 illustrate the wind roses obtained for wind speed and gust using observations and for all forecast horizons from model output respectively for ATPM, INVT, INVV, and MEVT. As can be seen in Figure 7, the predominant wind direction is Northeast and the second most frequent is North at ATPM Point. The model is completely capable of reproducing this pattern across all analyzed forecast horizons. However, there is an overestimation of the occurrences of high wind speeds and gusts from the main direction (Northeast). This overestimation pattern is also observed for the gust occurrences from North at this point.
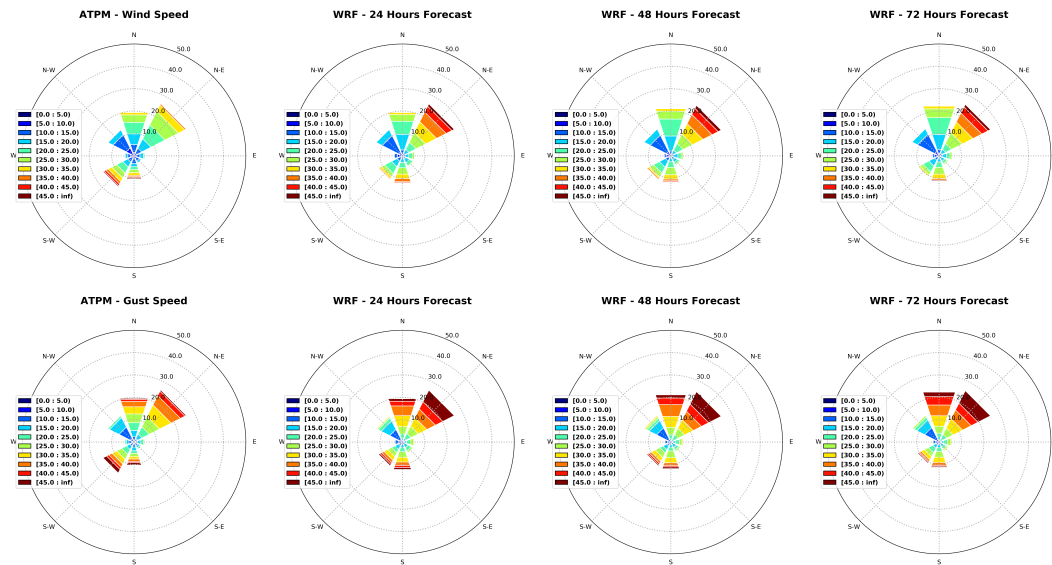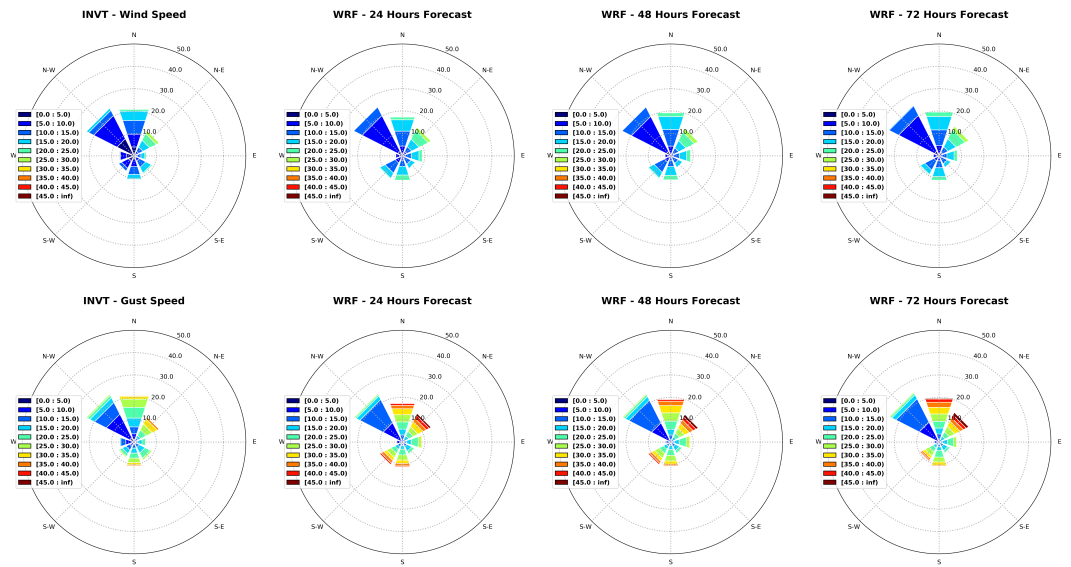
Figure 7. Wind roses built with observational data from the ATPM (left panels) and model output. The colors represent wind magnitude (upper panels) and gusts (lower panels) for forecast horizons of 24, 48, and 72 hours.

In general, the wind speed at INVT, INVV and MEVT are lower than at ATPM station. The predominant direction at INVT (Figure 8) is Northwest and the second most common is North. Again, the model represents well the main directions of winds occurrence. In general, it is apparent that the model tends to slightly underestimate the total number of wind occurrences from North at this point. Here, the Northeast and North gusts tend to be slightly overestimated. At INVV station (Figure 9), the main wind directions are North and Northeast. The model tends to overestimate mainly the wind gusts from Northeast. The remaining directions are well distributed and the model overestimates the wind occurrences from West. As there is no availability of wind gust observations at MEVT point, only wind speeds are analyzed in Figure 10. As evident from the observational data, over 25% of the winds propagate from the North, with the Northeast direction accounting for nearly 20%, and the Northwest direction representing approximately 15% of all occurrences. Despite the WRF model's tendency to underestimate the total occurrences of northward winds, it consistently identifies these three directions as the preferred wind patterns across all forecast horizons.

Figure 8. Wind roses built with observational data from the INVT (left panels) and model output. The colors represent wind magnitude (upper panels) and gusts (lower panels) for forecast horizons of 24, 48, and 72 hours.
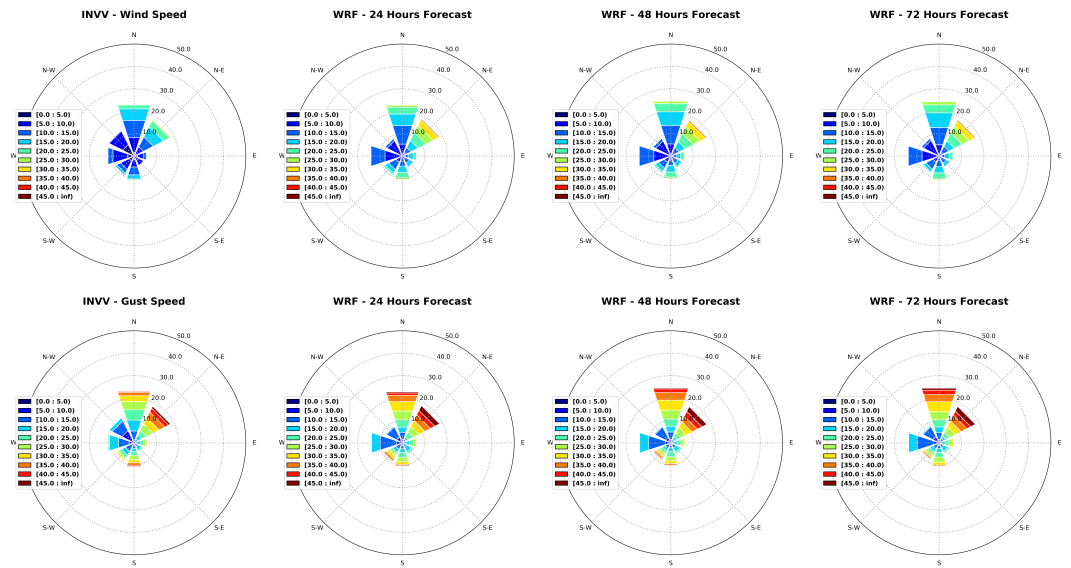
Figure 9. Wind roses built with observational data from the INVV (left panels) and model output. The colors represent wind magnitude (upper panels) and gusts (lower panels) for forecast horizons of 24, 48, and 72 hours.
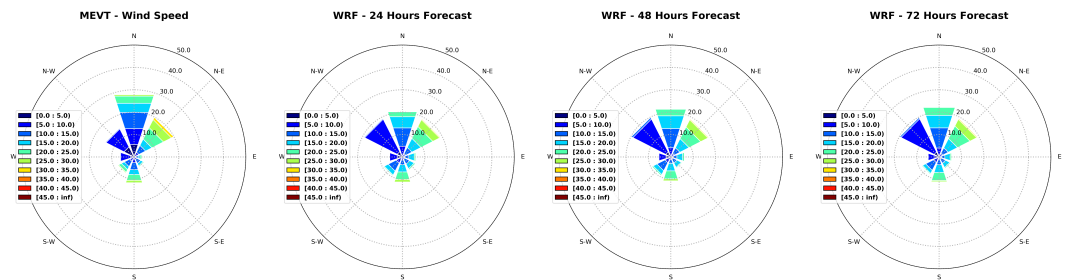
Figure 10. Wind roses built with observational data from the MEVT (left panels) and model output. The colors represent wind magnitude for forecast horizons of 24, 48, and 72 hours.

4. Discussion and Conclusions

This study aimed to identify the optimal set of physical parameterizations that better predicts the wind patterns during a severe wind event that occurred in the coastal region of the state of Espírito Santo. Subsequently, an evaluation of the year-long model simulation was carried out using the optimal parameterization set. This assessment considered forecast horizons of 24, 48, and 72 hours, and all simulations employed a high spatial resolution grid (1 km) with WRF model.

As seen in the results, the simulations conducted in the initial phase of this study considered changes in specific parameterization packages to assess the impact of each set of parameterizations on forecast quality. For instance, between tests T2 and T3, only the microphysics parameterization (MP) package was modified, and in this case, the observed differences were quite small, particularly in relation to wind speeds. Between tests T3 and T4, only the cumulus parameterization package was altered, and there was also little discernible difference in the results. Lastly, between tests T8 and T9, only the microphysics parameterization package was changed - however, in this case, the boundary layer (BL) package used in both simulations was MY-NN3, different from the one used in tests T2 and T3 (YSU). Although the differences in representing the August 2021 event in T8 and T9 were minimal, both simulations stood out with low correlation values and higher BIAS values compared to the other simulations, for both wind speed and gust. The best statistical indices for representing the event were obtained using the combination of Tiedtke (cumulus parameterization), Thompson for MP parameterization, TKE for boundary layer, Monin-Obukhov for surface layer, Unified-NOAH for land surface parameterization and RRTMG for both long and shortwave radiation (T1). This set of parameterizations excelled with the highest correlation values and the lowest BIAS values for both wind speed and gust representation.

The good results obtained with the T1 configuration are mainly related to the Tiedtke and Thompson parameterizations, which are recommended for regions with a high occurrence of cumulus clouds. For the prediction of wind magnitude and gusts, the accurate representation of convective processes is crucial due to the updrafts and downdrafts originating from these types of systems. The main advantage over the RRTM scheme for representing atmospheric radiative transfer is related to computational efficiency.

The results obtained from the one-year forecasting period demonstrate that WRF is capable of effectively representing the overall wind pattern, even up to three days in advance (72-hour forecast horizon). In general, the statistical metrics indicate a good performance of the model even for the 72-hour forecast horizon, with correlation coefficients always higher than 0.60 in all analyzed points. Naturally, as anticipated, the accuracy of the forecasts diminishes as the forecast horizon is extended. The best wind forecast performance was obtained for MEVT station, which exhibited correlation values above 0.73 and lower bias values for all three forecast horizons. But generally speaking, the model accurately predicts the frequency of winds in the primary direction but underestimates occurrences from the southwest at the ATPM station. At this same location, the model indicates stronger north winds than those recorded by the anemometer at this station.

Regarding the INVT station, the model accurately captures the directional wind pattern but overestimates the intensity of northeast gusts. At the INVV station, north winds are well-represented, and the occurrence of northeast winds is adequately depicted, despite a slight overestimation of wind speed and gusts in that direction. Although the model's representation of gusts at the MEVT station couldn't be assessed, the wind speed representation indicates that the forecasts effectively capture the wind pattern at this location, especially emphasizing south-wind occurrences. A slight underestimation (overestimation) of north and northeast (northwest) wind events is observed at this point.

The overall performance of the atmospheric forecasting, with a focus on coastal wind representation, was satisfactory. However, it is essential to acknowledge that the results obtained indicate room for improvement. Despite the high resolution of the employed grid (1 km), it becomes evident that the quality of the forecast results diminishes as we approach the ocean, aligning with one of

the conclusions drawn in the work done by XXX. In this regard, two aspects need attention as they have the potential to enhance the results: i) The specification of land use and land cover type; ii) The representation of sea surface temperature.

Concerning the first point, it is noted that the rapid urbanization, particularly in developing countries like Brazil, has contributed to changes in land cover types. Therefore, employing an updated database to delineate land use and land cover types in the area of interest has the potential to improve the overall performance of atmospheric modeling. Regarding the second point, given the degradation in result accuracy in areas closer to the sea, it is understood that an accurate representation of sea surface temperature (SST) is crucial for the correct simulation of atmospheric dynamics in a high-resolution model - of couse, the reverse is also true. Thus, it is believed that increasing the resolution of the sea surface temperature database used in the WRF model can significantly enhance result accuracy in coastal areas. Both of these aspects should be considered in the next steps to further enhance the high-resolution wind model.

References

1. Intergovernmental Panel on Climate Change (IPCC). Weather and Climate Extreme Events in a Changing Climate. In *Climate Change 2021 – The Physical Science Basis: Working Group I Contribution to the Sixth Assessment Report of the Intergovernmental Panel on Climate Change*; Cambridge University Press: Cambridge, England, 2023; pp. 1513–1766

2. Thomas, B.R.; Kent, E.C.; Swail, V.R.; Berry, D.I. Trends in ship wind speeds adjusted for observation method and height. *International Journal of Climatology* **2008**, *28*, 747-763.

3. Tokinaga, H.; Xie, S.-P. Wave and Anemometer-Based Sea Surface Wind (WASWind) for Climate Change Analysis. *Journal of Climate* **2011**, *24*, 267-285.

4. Young, I. R.; Zieger, S.; Babanin, A. V. Global Trends in Wind Speed and Wave Height. *Science* **2011**, *332*, 451-455.

5. Liu, Q.; Babanin, A. V.; Zieger, S.; Young, I. R.; Guan, C. Wind and Wave Climate in the Arctic Ocean as Observed by Altimeters. *Journal of Climate* **2016**, *29*, 7957-7975.

6. Ribal, A.; Young, I.R. 33 years of globally calibrated wave height and wind speed data based on altimeter observations. *Scientific Data* **2019**, *6*, 77.

7. Andrade, K. M; Pinheiro, H. R.; Neto, G. D. Extreme precipitation episode in Rio de Janeiro: Synoptic analysis, numerical simulation and comparison among previous events. *Ciência e Natura* **2015**, *37*, 175-180.

8. Freitas, A. A.; Oda, P. S. S.; Teixeira, D. L. S.; Silva, P. N.; Mattos, E. V.; Bastos, I. R. P.; Nery, T. D.; Metodiev, D.; Santos, A. P. P.; Gonçalves, W. A. Meteorological conditions and social impacts associated with natural disaster landslides in the Baixada Santista region from March 2nd–3rd, 2020. *Urban Climate* **2022**, *42*, 101-110.

9. Pereira Filho, A. J.; Pereira, J. D.; Vemado, F.; Silva, I. W. Operational Hydrometeorological Forecast System for Espírito Santo State, Brazil. *Journal of Hydrologic Engineering* **2015**, *22*.

10. Souza, N. B. P.; Nascimento, E. G. S.; Moreira, D. M. Performance evaluation of the WRF model in a tropical region: Wind speed analysis at different sites. *Atmósfera* **2021**, *36*, 253–277.

11. O.A.C. Amarante, F.J.L. Silva, P.E.P. Andrade, E. Parecy, *Atlas Eólico: Espírito Santo*, Agência de Serviços Públicos de Energia do Estado do Espírito Santo (ASPE), Vitória, 2009.

12. Oliveira, K. S. S.; Quaresma, V. S. Condições Típicas de Vento sobre a Região Marinha Adjacente à Costa do Espírito Santo. *Revista Brasileira de Climatologia* **2018**, *22*, 503-523.

13. Skamarock, W. C.; Klemp, J. B.; Dudhia, J.; Gill, D. O.; Barker, D.; Duda, M. G.; Powers, J. G. *A Description of the Advanced Research WRF Version 3*; National Center for Atmospheric Research, Boulder, Colorado, USA, 2008; (NCAR/TN-475+STR).

14. Skamarock, W. C.; Klemp, J. B.; Dudhia, J.; Gill, D. O.; Liu, Z.; Berner, J.; Wang, W.; Powers, J. G.; Duda, M. G.; Barker, D. M.; Huang, X.-Y. *A Description of the Advanced Research WRF Model Version 4.3*; National Center for Atmospheric Research, Boulder, Colorado, USA, 2021; (NCAR/TN–556+STR).

15. Skamarock, W. C.; Klemp, J. B.; Dudhia, J.; Gill, D. O.; Liu, Z.; Berner, J.; Wang, W.; Powers, J. G.; Duda, M. G.; Barker, D. M.; Huang, X.-Y. *A Description of the Advanced Research WRF Model Version 4*; National Center for Atmospheric Research, Boulder, Colorado, USA, 2019; (NCAR/TN–556+STR).

16. Tiedtke, M. A comprehensive mass flux scheme for cumulus parameterization in large-scale models. *Monthly Weather Review* **1989**, *117*, 1779-1800.

17. Thompson, G.; Field, P. R.; Rasmussen, R. M.; Hall, W. D. Explicit forecasts of winter precipitation using an improved bulk microphysics scheme. Part II: Implementation of a new snow parameterization. *Monthly Weather Review* **2008**, *136*, *12*, 5095-5115.

18. Janjic, Z. The step-mountain eta coordinate model: Further developments of the convection, viscous sublayer, and turbulence closure schemes. *Monthly Weather Review* **1994**, *122*, 927–945.

19. Tewari, M.; Chen, F.; Wang, W.; Dudhia, J.; Lemone, M. A.; Mitchell, K. E.; Ek, M.; Gayno, G.; Wegiel, J. W.; Cuenca, R. Implementation and verification of the unified NOAH land surface model in the WRF model. 20th conference on weather analysis and forecasting/16th conference on numerical weather prediction, American Meteorological Society, Seattle, WA, US, 14-01-2004.

20. Iacono, M. J.; Delamere, J. S.; Mlawer, E. J.; Shephard, M. W.; Clough, S. A.; Collins, W. D. Radiative forcing by long–lived greenhouse gases: Calculations with the AER radiative transfer models *J. Geophys. Res.* **2008**, *113*.

21. Kain, J. S. The Kain–Fritsch convective parameterization: An update. *J. Appl. Meteor.* **2004**, *43*, 170–181.

22. Hong, S.-Y.; Dudhia J.; Chen S.-H. A revised approach to ice microphysical processes for the bulk parameterization of clouds and precipitation. *Mon. Wea. Rev.* **2004**, *132*, 103–120.

23. Hong, S.–Y.; Noh, Y.; Dudhia, J. A new vertical diffusion package with an explicit treatment of entrainment processes. *Mon. Wea. Rev.* **2006**, *134*, 2318–2341.

24. Jimenez, P. A.; Dudhia, J.; Gonzalez–Rouco, J. F.; Navarro J.; Montavez, J. P.; Garcia–Bustamante, E. A revised scheme for the WRF surface layer formulation. *Mon. Wea. Rev.* **2012**, *140*, 898–918.

25. Niu, G.–Y.; Yang, Z.-L.; Mitchell, K. E.; Chen, F.; Ek, M. B.; Barlage, M.; Kumar, A.; Manning, K.; Niyogi, D.; Rosero, E.; Tewari, M.; Xia, Y. The community Noah land surface model with multiparameterization options (Noah–MP): 1. Model description and evaluation with local–scale measurements. *J. Geophys. Res.* **2011**, *116*.

26. NOAA, cited 2001: National Oceanic and Atmospheric Administration Changes to the NCEP Meso Eta Analysis and Forecast System: Increase in resolution, new cloud microphysics, modified precipitation assimilation, modified 3DVAR analysis. [Available online at http://www.emc.ncep.noaa.gov/mmb/mmbpll/eta12tpb/.]

27. Grell, G. A.; Devenyi, D. A generalized approach to parameterizing convection combining ensemble and data assimilation techniques. *Geophys. Res. Lett.* **2002**, *29*.

28. Chen, S.-H.; Sun, W.-Y. A one-dimensional time dependent cloud model. *J. Meteor. Soc. Japan.* **2002**, *80*, 99–118.

29. Hong, S.–Y.; Lim, J.–O. J. The WRF single–moment 6–class microphysics scheme (WSM6). *J. Korean Meteor. Soc.* **2006**, *42*, 129–151.

30. Grell, G. A. Prognostic Evaluation of Assumptions Used by Cumulus Parameterizations *Mon. Wea. Rev.* **1993**, *121*, 764–787.

31. Mlawer, E. J.; Taubman, S. J; Brown, P. D.; Iacono, M. J.; Clough, S. A. Radiative transfer for inhomogeneous atmospheres: RRTM, a validated correlated–k model for the longwave. *J. Geophys. Res.* **1997**, *102*, 16663–16682.

32. Dudhia, J. Numerical study of convection observed during the Winter Monsoon Experiment using a mesoscale two–dimensional model. *J. Atmos. Sci.* **1989**, *46*, 3077–3107.

33. Nakanishi, M.; Niino, H. An improved Mellor–Yamada level 3 model: its numerical stability and application to a regional prediction of advecting fog. *Bound. Layer Meteor.* **2006**, *119*, 397–407.

34. Ferreira, R. C.; Alves Junior, M. P.; Vendrasco, E. P.; Aravequia, J. A.; Nolasco Junior, L. R.; Biscaro, T. S. Impacto das Parametrizações de Microfísica na Previsão de Precipitação utilizando Assimilação de Dados de Radar. *Revista Brasileira de Meteorologia* **2020**, *35*, 123-134.

35. Iacono, M. J. Application of improved radiation modeling to general circulation models. *Atmospheric and Environmental Research* **2011**.